Ann. Geophysicae 16, 148–160 (1998)

Annales Geophysicae

Simultaneous measurements of X-rays and electrons during a pulsating aurora

N. Østgaard[1], J. Stadsnes[1], K. Aarsnes[1], F. Søraas[1], K. Måseide[2], M. Smith[3], J. Sharber[4]

[1] Department of Physics, University of Bergen, Allegaten 55, N-5007 Bergen, Norway
[2] Department of Physics, University of Oslo, P.O.Box 1048 Blindern, N-0316 Oslo, Norway
[3] Laboratory for Extraterrestrial Physics, NASA/GSFC, Greenbelt, MD 20771
[4] Southwest Research Institute, 6220 Culebra Rd., San Antonio, USA

Received: 21 January 1997 / Revised: 28 August 1997 / Accepted: 2 September 1997

Abstract. The PULSAUR II rocket was launched from Andøya Rocket Range at 23.43 UT on 9 February 1994 into a pulsating aurora. In this paper we focus on the observations of precipitating electrons and auroral X-rays. By using models it is possible to deduce the electron energy spectrum from X-ray measurements. Comparisons are made between the deduced electron fluxes and the directly measured electron fluxes on the rocket. We found the shape of the observed and the deduced electron spectra to fit very well, with almost identical e-folding energies in the energy range from 10 keV to ~60–80 keV. For the integrated fluxes from 10.8 to 250 keV, we found a discrepancy of 30% . By combining two models, we have found a good method of deducing the electron precipitation from X-ray measurements. The discrepancies between calculations and measurements are in the range of the uncertainties in the measurements.

Key words Ionospheric particle precipitation · Magnetospheric physics · Annual phenomena · Energetic particle

1 Introduction

Pulsaur II was a sounding rocket aimed at the study of generating mechanisms of pulsating aurora and related ionospheric effects. The rocket was equipped with instruments to measure electrons and ions over a wide range of energies and pitch angles, optical emissions and X-rays, DC and AC electric and magnetic fields, HF emissions, and electron densities and temperatures (Måseide *et al.*, 1995; Søraas *et al.*, 1995; Stadsnes *et al.*, 1995).

In this paper we will focus on the X-rays and the electron measurements. By the combined use of two models, Berger and Seltzer (1972), Seltzer and Berger (1974) and Walt *et al.* (1979), it is possible to deduce the electron precipitation that produces the measured X-rays, and make a comparison between the measured and the deduced electron fluxes.

Precipitating electrons deposit their energy into the atmosphere by ionization, excitation, heating of the neutral gas and X-ray bremsstrahlung. X-rays are produced by high-energy primary electrons, while the other energy depositions involve both primary and secondary electrons over a wide energy range. The number of X-ray photons (n) that are generated by an electron with an initial energy (E_e) slowing down in the atmosphere, is rather small. For example, $n(200\ \text{keV}) = 0.0052$ and $n(20\ \text{keV}) = 0.000057$ (Berger and Seltzer, 1972). Nevertheless, X-ray measurments are very useful in the study of the electron precipitation. One advantage is that X-rays can be detected remotely, and information about the spectra, as well as spatial and temporal structures in the electron precipitation, can be obtained. Another advantage is that X-rays can be detected in daylight. Compared to other remote-sensing techniques like UV and visible imaging, based on emissions resulting mostly from the soft part of the electron spectrum, the X-rays are produced by high-energy electrons giving information on the energetic precipitation (Robinson and Vondrak, 1994). This makes X-ray measurements favourable in the study of energetic electron precipitation.

As balloon and rocket experiments have recorded auroral X-rays since about 1960, there has been a need for models that calculate the X-ray production from electron precipitation. Several models using different approximations and simplifications have been developed in order to calculate the yield of X-rays from electron spectra (Rees, 1964; Kamiyama, 1966; Freyer, 1969; Berger *et al.*, 1970; Berger and Seltzer, 1972; Seltzer and Berger, 1974; Luhman and Blake, 1977; Walt *et al.*, 1979; Khosa *et al.*, 1984; Robinson *et al.*, 1989; Gorney, 1987). Experiments have been performed to make simultaneous measurements of electrons and X-rays

(Vij *et al.*, 1975; Mizera *et al.*, 1978; Goldberg *et al.*, 1982; Datlowe *et al.*, 1988), and the comparisons between measured and calculated X-rays have resulted in different degrees of agreement. Generally, the discrepancies have been of a factor between 2 and 10.

In this paper a combination of two models is used. One model, developed on Berger and Seltzer (1972) and Seltzer and Berger (1974), is used to calculate the X-rays emitted into the upward hemisphere from a horizontal production layer. To take into account the angular distribution of X-rays escaping the atmosphere, we have used another model, developed by Walt *et al.* (1979). Taking into account both scattering and absorption, these models make it possible to calculate both the angular scattering and the energy decrease resulting from the Compton effect. Although these two models also contain approximations and simplifications, the works of Berger and Seltzer and Walt *et al.* appear to be the best so far. Combined with the work of Mæhlum and Stadsnes (1967) which accomplishes the transposition from anisotropic to equivalent isotropic electron fluxes, these models constitute a complete method to derive equivalent isotropic fluxes and energy spectra for the angular-dependent precipitating electrons from angular-dependent X-ray measurements. Our study demonstrates the possibility to deduce the electron precipitation from X-ray measurements with a high degree of accuracy.

2 The rocket experiment and launch conditions

Pulsaur II was launched from the Andøya Rocket Range, Norway, into a pulsating aurora on 9 February 1994 at 23.43 UT (01.23 MLT), during the recovery phase of an auroral substorm.

From the ground-based measurements of the magnetic field and all-sky TV recordings, we see that an auroral substorm breakup occurred at about 21.55 UT. The visual aurora brightened and expanded northwards. During the next hours strong magnetic activity and several intense auroral events were observed. At about 23.10 UT the H component of the magnetic field showed the strongest negative bay ($\Delta H = -1000$ nT), and when the rocket was launched we measured $\Delta H = -656$ nT. During the flight ΔH decreased to -525 nT. Pulsaur II was launched early in the recovery phase of the substorm.

Arc fragments and patches covered the whole sky, and strong pulsations were seen. The main structures moved slowly from the south-west to the north-east, while smaller structures moved more rapidly from south-east to north-west. In Fig. 1 the geometry of the observations and orientation of the detectors are shown as well as the production layer for the X-rays.

The *X-ray detector* was a 1-mm thick NaI(Tl) scintillation crystal with a photomultiplier tube. A collimator defined the opening angle (16° FWHM) and a broom magnet prevented the penetration of high-energy electrons (up to about 200 keV) into the detector. There were seven differential energy channels from 5.6 up to 35.4 keV. In addition there was an integral energy channel detecting energies >35.4 keV. At 100 keV the scintillator detection efficiency was 45%. The X-rays measured by this detector are produced by electrons with energy greater than 5.6 keV.

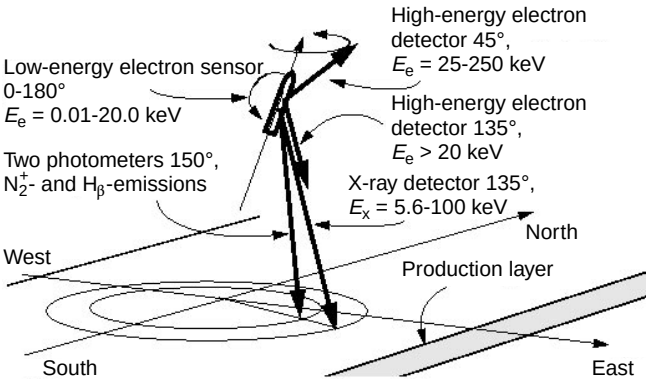

Fig. 1. Geometry of the observations and orientation of the instruments on board the rocket; the X-ray production layer is indicated

The two *photometers* with opening angles of about 8° (FOV) measured N_2^+ and H_β emissions. In this paper the measurements of the N_2^+ emissions at 427.8 nm are used. This emission has been found to be a good indicator for the energy flux of the precipitating electrons (Bryant *et al.*, 1970; Omholt, 1971). As this is a prompt emission, the N_2^+ measurements are very suitable for comparison with the X-ray fluxes that are also produced immediately. The electrons <5–10 keV dominate in the excitation of this emission, since they usually give much higher energy deposited into the atmosphere than the >10-keV electrons.

The X-ray detector and the photometer respond to precipitating electrons in different spectral ranges, and together they cover a wide electron energy range.

The X-ray detector was looking at 135° and the photometer was looking at 150° to the rocket axis. As the rocket was spinning we achieved measurements from these two detectors in all azimuth angles. The spin period of the rocket was 0.5 s. As the sampling time was 6.5 ms, we got about 80 samples per spin. This gives us information about both temporal variations and spatial structures in the source region of the X-rays and the N_2^+ emissions during the whole flight.

The two *high-energy electron detectors* (HEED) were looking at 45° and 135° relative to the spin axis. They both used Si solid-state detectors. The detector looking at 135° to the spin axis worked quite well up to 73-s flight time, but then the fluxes became too large and the detector saturated. The backscattered electron energy spectra above 20 keV could be measured before saturation. From the detector looking at 45° to the spin axis we obtained integral count rates of precipitating electrons with energies above 25 keV with a time resolution of 257 ms.

The *low-energy electron sensor* (LEES) was a "top hat" electrostatic analyser based on a similar instrument (Sharber *et al.*, 1988) but differing in a number of

aspects, including the use of MCPs instead of channeltrons. Twenty-four sensors were covering all directions relative to the spin axis. The opening angle for each sensor was 15 (FWHM). Each sensor had 32 energy channels ranging from 10 eV up to 20 keV. The energy resolution was 26%. A programmable high-voltage unit stepped the voltage simultaneously for all the sensors, resulting in measured energy spectra (10 eV–20 keV) from all sensors every 288 ms. Consequently, we obtained energy spectra at nearly all pitch angles from 0° to 180°. The LEES detector provided data from about 135 to 350 s flight time.

3 Observations

Before we present our observations, some remarks concerning the X-ray measurements are required. During the flight minimum ionizing particles contaminated the X-ray detector. As the energy deposited by these particles only depends on the thickness of the scintillation crystal, the energy deposition peaked around 30 keV, resulting in observable count rates only in the two uppermost energy channels. The estimation of the background count rates are based upon a statistical analysis. By studying the count rates during the whole flight in all azimuth sectors, we found that the count rates sometimes dropped down to zero in all the energy channels except for the two uppermost channels. These count rates, which are only observed in the integral channel (>35.4 keV: 4 counts/26 ms) and the upper differential channel (20.8–35.4 keV: 1 count/26 ms), cannot be auroral X-rays produced by electron precipitation but must neither be due to a stable energetic background source like minimum ionizing particles, and are consequently subtracted. The count rates from these minimum ionizing particles are about 10% of the average total count rates in each channel.

In Fig. 2 an overview plot for the whole flight is shown. In the upper panel the count rates from HEED (electrons from 25 to 250 keV) are plotted, with a time resolution of 257 ms. In the middle panel, X-ray count rates (10 to 35.4 keV) are plotted, and in the bottom panel the N_2^+ measurements are plotted. The X-ray and the N_2^+ emission panels are plotted for all azimuth angles.

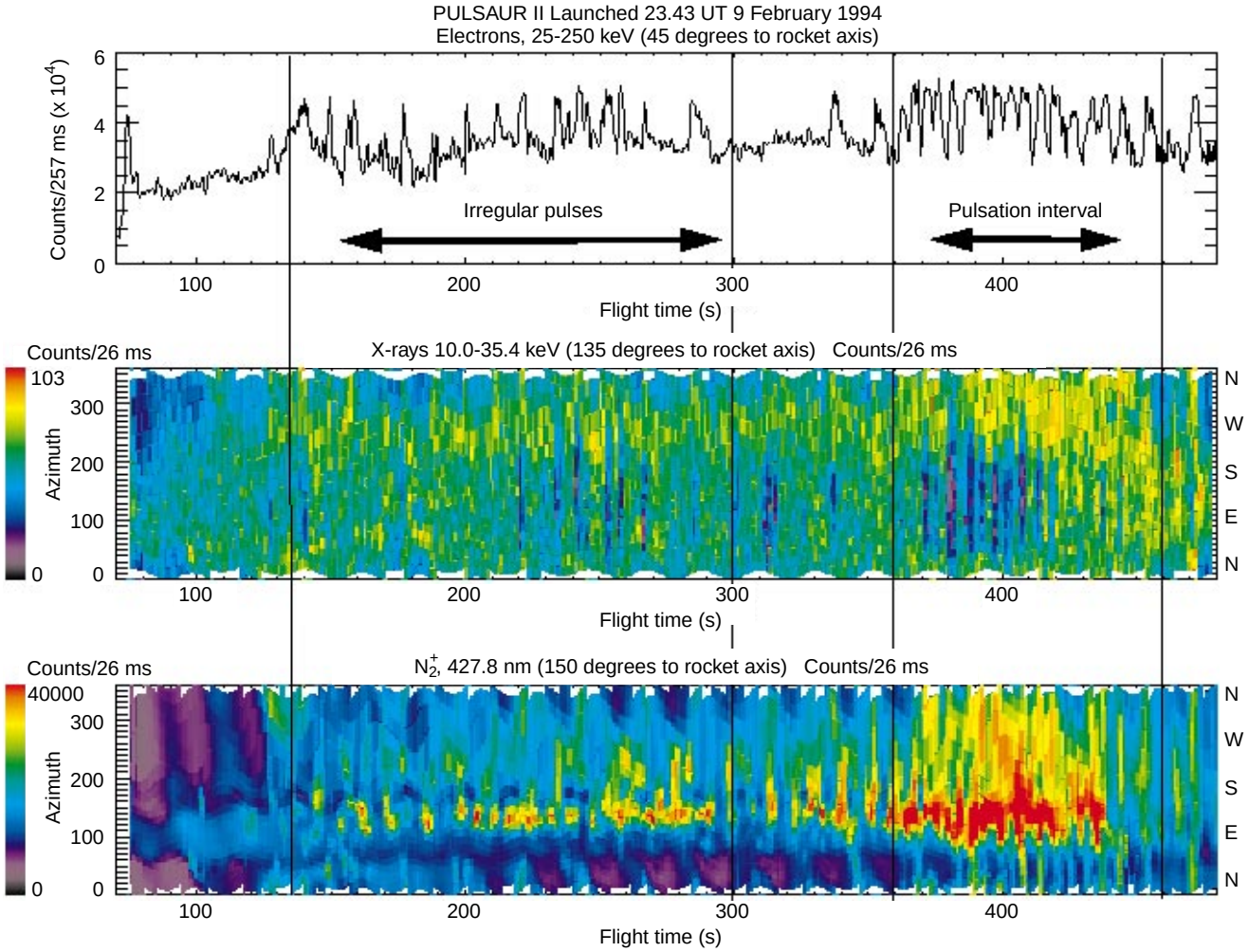

Fig. 2. Electrons (counts/257 ms): $25 < E_e < 250$ keV, X-rays (counts/26 ms): $10.0 < E_x < 35.4$ keV and N_2^+ emissions (counts/26 ms) during the whole flight

Irregular and isolated single pulses were observed during the time-interval from 125 to 300-s flight time. Continuous and more regular pulsations were observed during the time-interval from 360 to 460-s flight time, with typical periods of 3 to 9 s. These intervals are indicated in Fig. 2.

The most intense X-rays occurred in the north-west while the most intense N_2^+ emissions occurred in the south-east. The pulses and the pulsations were observed most clearly in the south for both the X-rays and the N_2^+ emissions appearing to be in phase with each other.

Before a comparison between the directly measured and the calculated electrons based on the X-ray measurements can be made, we must make sure that the electron detector and the X-ray detector measure the same structures. If it is possible we ought to demand measurements at the same intensity of electron precipitation. From the ground, all-sky TV recordings of the aurora were obtained for the whole flight. By studying the all-sky pictures we found that the time-interval from 135 to 199-s flight time, and the azimuth sector 0° to 30°, properly satisfy these conditions. As we want to make use of all available data, we have chosen a time-interval when LEES was operating, although the most clear pulsations were seen later in the flight.

In Fig. 3 the all-sky picture at 158-s flight time is shown. One pixel covers an area of about 2×2 km. The scanning paths of the X-ray detector and the photometers projected down to the horizontal production layer, assumed to be located at 110 km height, are indicated, as is the azimuth sector 0°–30°. The rocket position projected down to the production layer along the field line is also indicated. At this time-interval and in this azimuth sector it is seen that the X-ray detector and the photometers are looking close to the rocket position, projected down to the production layer, and measuring the same structures in the aurora.

In Fig. 4 this azimuth sector is indicated in the X-rays and N_2^+ emission panels. As irregular pulsations were observed in this time-interval, it is possible to examine the degree of correlation between the different measurements. The pulse maxima are marked in the figure and indicate some correlation between the three panels. This correlation will be discussed in Sect. 5.

Concerning the intensity, there are some uncertainties. The sensitivity in the all-sky TV recording is too rough to determine the intensity exactly. Furthermore, the strongest intensity of light and X-rays did not appear in the same azimuth sectors at the same time (Fig. 2). So, when the all-sky pictures are used for choosing the azimuth sector and the time-interval, we only know that we measure at roughly the same intensity of light. But we do not know if this would be so with respect to the X-ray intensity.

As a conclusion so far, the detectors measure the same auroral structures, but we do not know if we have uniform energetic electron precipitation into an area covering both the rocket position and the azimuth sector where the X-ray detector is looking. This must be kept in mind when the comparison between the X-rays and the electrons is made.

4 The models

Two consistent production models are used to deduce the electron spectra from the measured X-ray spectra. The first model was developed by Berger and Seltzer (1972) and Seltzer and Berger (1974), and the second model by Walt *et al.* (1979). These models are used to calculate the X-ray bremsstrahlung produced by energetic electrons that precipitate into the atmosphere. The calculations in both the models take into account:

The multiple scattering and slowing down of electrons. Both elastic and inelastic interactions with nuclei and orbital electrons in the atmosphere are taken into account. This includes the production of knock-on electrons as well.

Concerning the X-rays, both the multiple Compton scattering (angular scattering and energy decrease) and photoelectric absorption are taken into account.

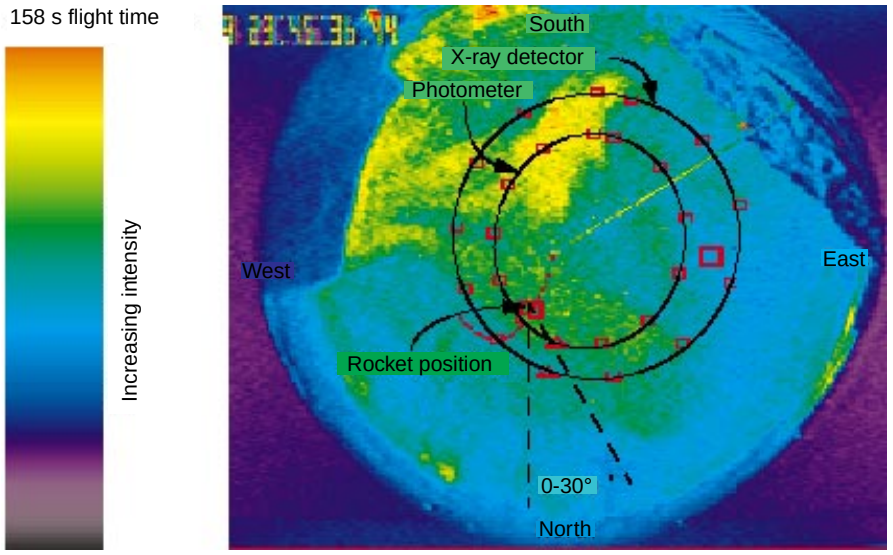

Fig. 3. All-sky TV picture at 158-s flight time. Projections down to the horizontal production layer are indicated for the scanning paths of the X-ray detector and the photometers, and down along the field line for the rocket position. The *yellow streak* in SE is produced by a lidar beam. The *small red squares* are the centre field of view at each centre time of data accumulation for the photometer and the X-ray detector. The *large red square* indicates the location of EISCAT

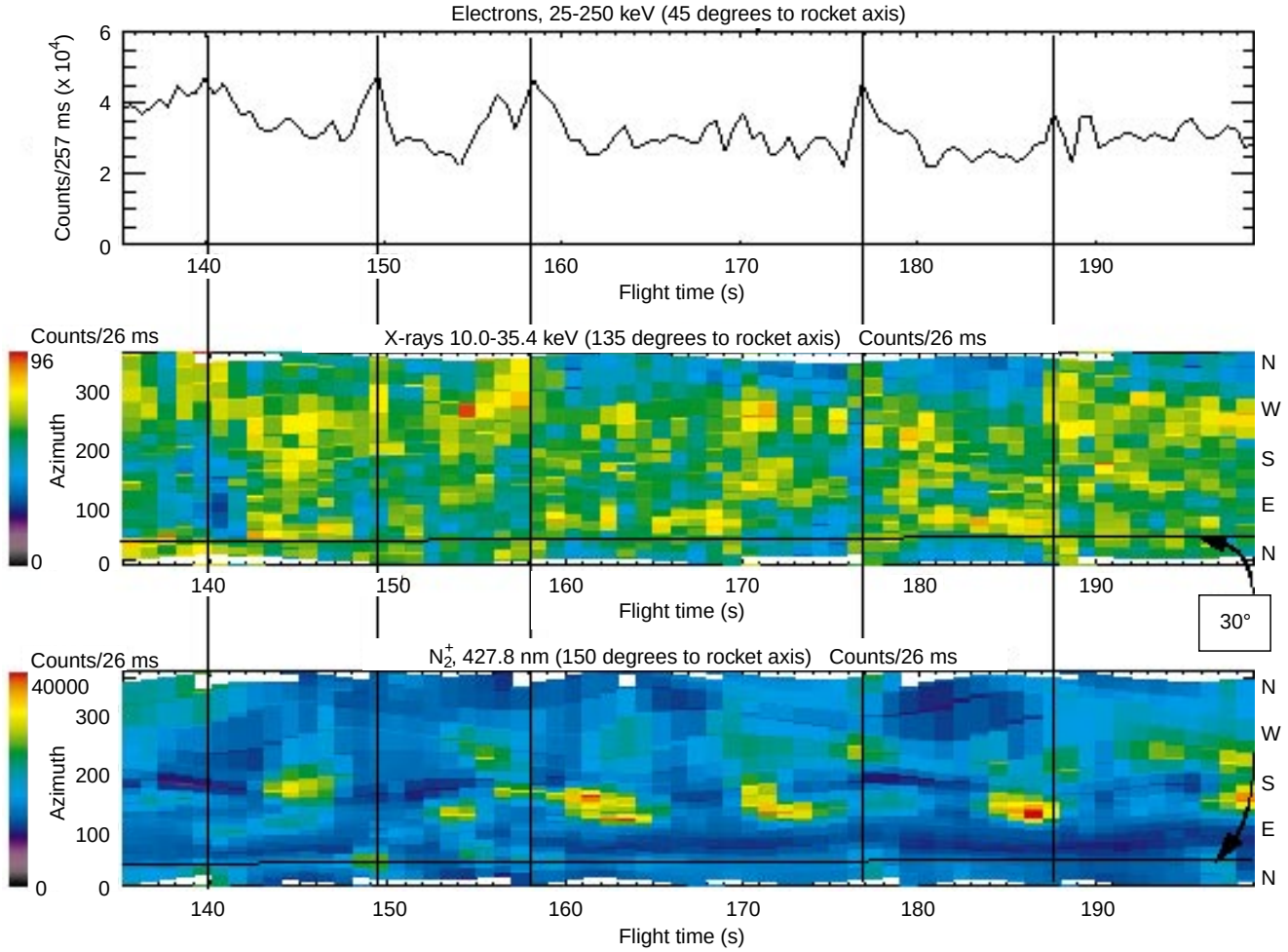

Fig. 4. Electrons (counts/257 ms): $25 < E_e < 250$ keV, X-rays (counts/26 ms): $10.0 < E_x < 35.4$ keV and N_2^+ emissions (counts/26 ms) for the time-interval 135–199-s flight time

The coherent or elastic scattering (Thomson scattering) is included in the work of Walt *et al.* but ignored by Berger and Seltzer. This is critical only for energies below 10–15 keV, where the photoelectric absorption dominates anyway and does not cause significant differences between the two models. As we have restricted our calculations to the energy range from 10.8 up to 250 keV, this will not influence the results presented in this paper to a large extent.

The models are based on the following assumptions and simplifications:

An isotropic electron flux into the atmosphere.

The precipitation of electrons into the atmosphere takes place uniformly over a wide area.

Monoenergetic beams of electrons generate X-rays only in a narrow altitude sheet in the atmosphere.

While Berger and Seltzer calculated the X-rays emitted in the upward hemisphere from each unit horizontal area of the production layer, Walt *et al.* calculated the X-ray fluxes out of the atmosphere at specific angles relative to nadir. By applying both models to our study we were able to take into account the fact that the X-ray detector was looking down on the production layer at specific slant angles.

To calculate the yield of X-rays from electrons, the model of Berger and Seltzer uses a Monte Carlo simulation based on analytical multiple scattering theories and the assumptions already mentioned. Walt *et al.* used analytic solutions to calculate the production of X-rays, giving almost identical results to the Monte Carlo model of Berger and Seltzer.

To calculate the penetration of the X-rays through the atmosphere, the scattering effects and photoelectric absorption were taken into account by a Monte Carlo simulation in both models.

Assuming an exponential shape of the electron energy spectrum, Seltzer and Berger calculated the resulting spectrum of the X-rays above the atmosphere, as shown in Fig. 5 (Seltzer and Berger, 1974). As seen, these spectra are also approximately exponentials. We have used a simple exponential to represent these X-ray spectra. As the lower part of these spectra are used to calculate the X-ray e-folding energies, we get a slight overestimate for the effective electron e-folding energies for high energies. The error introduced will be discussed.

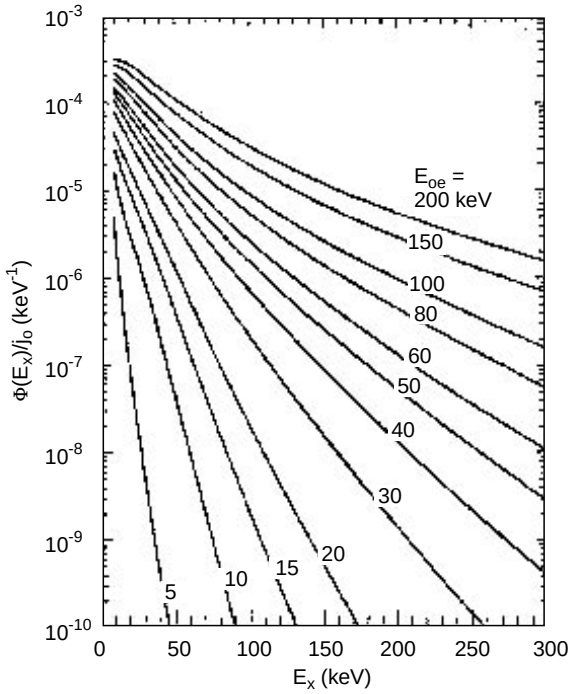

Fig. 5. The X-ray energy spectrum, $\Phi(E_x)/j_o$, normalized to incident integral electron flux (j_o), produced by different exponential electron distributions, calculated from the electron differential energy spectra. E_{oe} is the electron e-folding energy (Seltzer and Berger, 1974)

From Fig. 5, we find the X-ray spectrum $\Phi(E_x)/j_o$ emitted in the upward hemisphere from each unit horizontal area of the production layer as a function of electron e-folding energy and normalized to the incident integral electron flux (j_o).

Then we apply the model of Walt *et al.* (1979) to find the X-ray yield in the direction of the FOV of our X-ray detector. In our chosen azimuth sector (0°–30°) and time-interval (135–199-s flight time) the detector was looking at X-rays coming up at elevation angles of 33.4° to 54.3°. The centre elevation angle is close to 45°, which corresponds to 135° nadir angle in the model of Walt *et al.* (1979)

In Fig. 6 the X-ray spectra produced by electrons with an e-folding energy of 20 keV, calculated by Walt *et al.* (1979), are shown. The X-rays emitted at five different nadir angles are calculated showing a factor-10 increase in the X-ray flux going from 180° to 110° nadir angle.

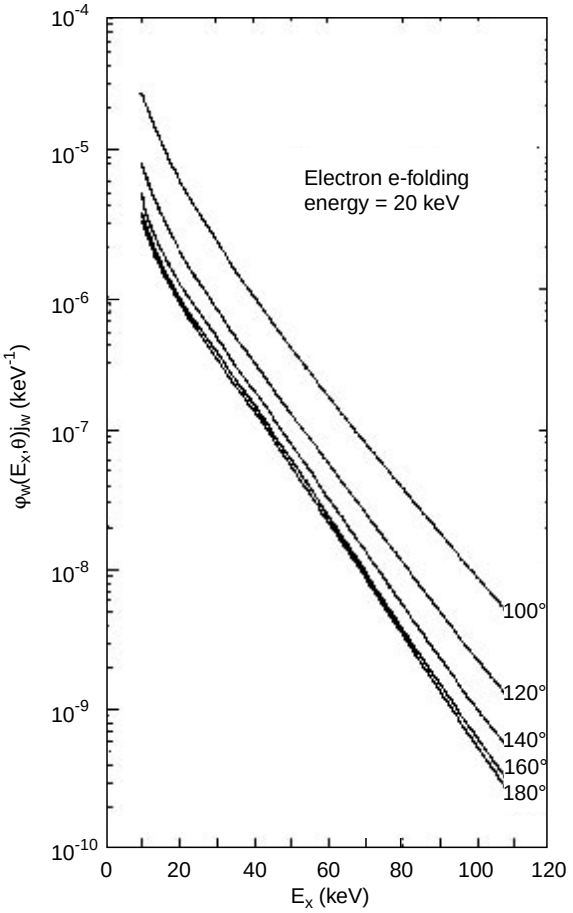

Fig. 6. Differential X-ray flux normalized to unit directional incident integral electron flux $\varphi_w(E_x,\theta)/j_w$, produced by an exponential electron distribution with an e-folding energy of 20 keV, for nadir angles 100°, 120°, 140°, 160° and 180° (Walt *et al.*, 1979)

In Table 1 the X-ray fluxes at 50 keV, normalized to incident integral electron fluxes, are listed for five different electron e-folding energies. From Berger and Seltzer we have found the calculated X-ray flux integrated over the upward hemisphere, and from Walt *et al.* we have found the calculated X-ray fluxes at 135° nadir angle.

Since Walt *et al.* calculated the directional X-ray fluxes at specific nadir angles and Berger and Seltzer calculated the X-ray fluxes in the upward hemisphere per unit horizontal area, the values from Berger and

Table 1. The X-ray fluxes at 50 keV normalized to unit-directional incident integral electron fluxes. $[\Phi(50\,\text{keV})/j_o]$ are from the work of Berger and Seltzer and $[\varphi_w(50\,\text{keV}, 135°)/j_w]$ are from the work of Walt *et al.* The column to the right gives the ratio, i.e. the reduction factor for each electron e-folding energy going from X-ray fluxes isotropically emitted into the upward hemisphere to X-ray fluxes at 135° nadir angles

Electron e-folding energy (keV)	$[\Phi(50\,\text{keV})/j_o]$ (keV^{-1}) Berger and Seltzer	$[\varphi_w(50\,\text{keV}, 135°)/j_w]$ (keV^{-1}) Walt *et al.* 135°	Ratio berger and Seltzer/ Walt *et al.* 135°
10	4.7×10^{-8}	2.6×10^{-9}	18.1
20	1.3×10^{-6}	9.5×10^{-8}	13.7
50	1.3×10^{-5}	1.2×10^{-6}	10.8
100	4.1×10^{-5}	8.9×10^{-6}	4.6
200	1.0×10^{-4}	1.6×10^{-5}	6.3

Seltzer must be divided by π to be comparable to the values calculated by Walt *et al.* (1979). In Fig. 7 the reduction factors are plotted as a function of electron e-folding energy. We have interpolated linearly between our five values.

5 Applying the model to our study

Based on the data from the LEES detector, we derived the electron spectra from 0.1 up to 20 keV. As we only obtained integral count rates from the HEED detector above 25 keV, we estimated the spectrum above 20 up to $\sim$250 keV, assuming that the spectrum in this range could be represented by an exponential function. As we have no spectral measurements above 20 keV, our approach will be to make this assumption and discuss the possibility of other shapes of the spectrum after the calculations and comparison have been made. This will be discussed in Sect. 6.

In order to satisfy the requirements concerning the input parameters used in the models, we have carried out some calculations. First, we reconstructed a pitch angle distribution for the HEED data, assuming this distribution to be identical to the pitch angle distribution of the electrons from 13.8 to 22.6 keV measured by the LEES detector (the energy range of the two uppermost channels in the detector).

Second, we calculated a full pitch angle distribution for the intermediate energy interval from 22.6 to 25.0 keV assuming exponential energy spectra above 20.0 keV.

In Fig. 8 we see that the pitch angle distributions for electrons at 9.6 and 20.0 keV are obviously anisotropic.

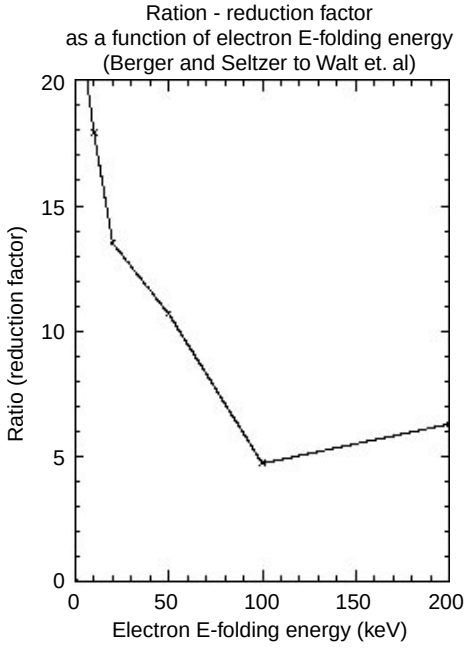

Fig. 7. The reduction factor for calculating the X-rays emitted at 135°, nadir angle (Walt *et al.*, 1979) from the X-rays emitted into the upward hemisphere (Seltzer and Berger, 1974). The reduction factor is interpolated linearly between our five values from Table 1

As the models are based upon the assumption of isotropic electron precipitation in the downward hemisphere, we have eliminated this source of discrepancy by calculating an equivalent isotropic distribution, i.e. the isotropic distribution that results in the same energy deposition in the atmosphere as the anisotropic distribution. In this calculation we have taken into account the backscattering of the electrons as a function of different pitch angles assuming that the 20-keV electrons can represent the whole distribution. From Mæhlum and Stadsnes (1967) we find the percentage of absorbed 20-keV electrons at 30°, 60° and 80° pitch angles. Interpolating between these values, we get the values in Table 2. The effect of an isotropic flux crossing a horizontal unit area is considered as well.

After proceeding in this way, we are able to use the X-ray measurements from 10.8 up to 100 keV to deduce the electron spectra above 10.8 keV and compare with the equivalent isotropic electron flux spectra deduced from measured electrons from 10.8 up to 250 keV.

6 Calculation of electrons from X-ray measurements

In deducing the electron spectra from the X-ray spectra, we have used a sum of two exponential functions using a least-squares method to represent the measured X-rays, according to Eq. (1):

$$\varphi(E_x, 135) = \varphi_{o1} \exp[-(E_x / E_{o1x})] + \varphi_{o2} \exp[-(E_x / E_{o2x})] \ , \quad (1)$$

From the modelled X-ray spectra in Fig. 5, we have calculated the X-ray e-folding energy, E_{ox}, as a function of electron e-folding energy for $E_{oe} = 0$ up to 200 keV. Interpolating using a third-order polynomial approximation and using the X-ray e-folding energy as the abscissa, we get the plot in Fig. 9, upper panel. As we have represented the X-ray spectra obtained by Seltzer and Berger (1974) by a simple exponential and used the lower part of the X-ray spectra to calculate the X-ray e-folding energies, the slope of the graph should not be as steep as shown in this panel. For the high energies we get a slight overestimate of the electron e-folding energies. In Fig. 9, lower panel, the same calculation is carried out for the X-ray flux produced at 10 keV as a function of X-ray e-folding energy, E_{ox}. This flux is normalized to the incident integral electron flux and reduced to get the flux at 135° nadir angle, giving $[\varphi_w(E_{ox}, 10, 135°)/j_w]$. It should be noted that X-ray flux at 10 keV is almost independent of the spectral hardness for electron e-folding energies, $E_{oe} > 25$ keV, because the expected increase in the X-ray flux due to the harder electron spectrum is partly cancelled out by the increasing preference of horizontal escape for increasing X-ray energies. From these panels we find the E_{oe} and $[\varphi_w(E_{ox}, 10, 135°)/j_w]$, when we have found E_{ox} from the measurements.

By following the procedure and using the equations described by Berger and Seltzer (1972), the differential electron flux calculated at 0 keV, η_{co}, is given by Eq. (2):

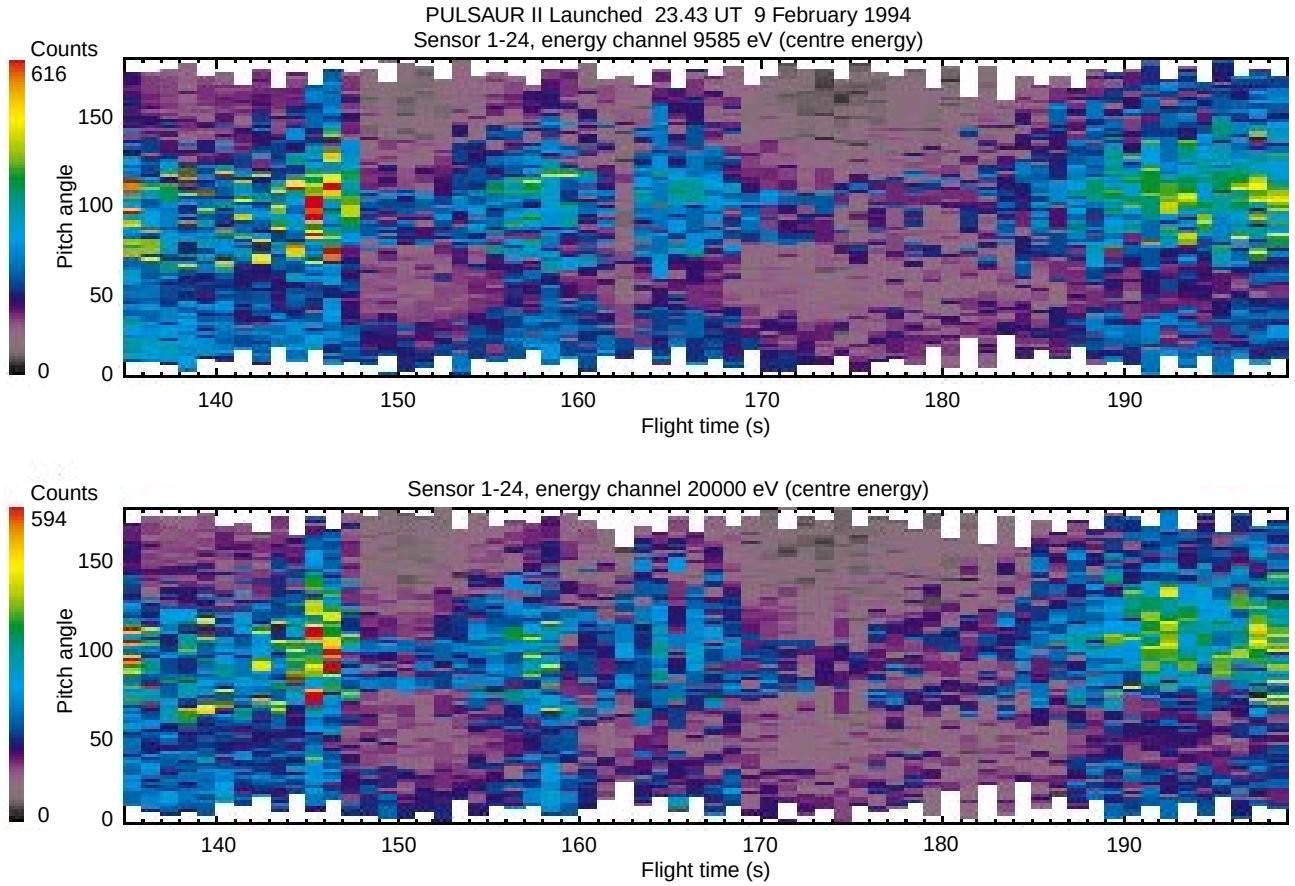

Fig. 8. Pitch angle distribution for electrons measured by the LEES detector: 9.6 and 20.0 keV (centre energies of the channels)

Table 2. Absorbed 20-keV electrons (Mæhlum and Stadsnes, 1967)

$\alpha_1 - \alpha_2$	Absorbed electrons 20 keV (%)
0°–10°	86
10°–20°	85
20°–30°	83
30°–40°	80
40°–50°	75
50°–60°	67
60°–70°	56
70°–80°	40
80°–90°	25

$$\eta_{\mathrm{co}} = \frac{j_{\mathrm{o}}}{\pi E_{oe}} = \frac{j_w}{E_{oe}} = \frac{\varphi(10, 135°)}{[\varphi_w(E_{\mathrm{ox}}, 10, 135°)/j_w] E_{oe}} \quad . \tag{2}$$

The integral electron flux from 10.8 to 250 keV is then given by Eq. (3):

$$\eta_{\mathrm{c}}(10.8 < E_x < 250, \theta) = \int_{10.8}^{250} \eta_{\mathrm{co1}} \exp[-(E_e / E_{\mathrm{o1}e})] + \int_{10.8}^{250} \eta_{\mathrm{co2}} \exp[-(E_e / E_{\mathrm{o2}e})] \ , \tag{3}$$

In Fig. 10 the X-ray spectra measured at 167- and 175-s flight time are shown in the two upper panels. Each of the two exponential approximations are shown by the dotted lines, and the dashed line shows the superimposed spectrum. In the bottom panel the calculated (dotted lines) and measured (solid line) electron spectra ($E_e > 10$ keV) are plotted. Comparing the measured and the deduced electron fluxes, we find that the shape of the spectrum and the magnitude of the fluxes coincide quite well up to ~60–80 keV, but above this energy we get a hard tail resulting from the hard tail in the measured X-rays. As we used only one exponential function to represent the electron integral count rates above 25 keV, this hard tail will not be present in the deduced spectra from the electron measurements.

The results of the comparison between integral fluxes deduced from measured electrons and calculated integral electron fluxes from differential X-ray spectra, are shown in Fig. 11.

The main results from Figs. 10 and 11 are listed in Table 3.

In the third panel of Fig. 11, where the directly measured X-rays and the directly measured electrons are compared, we get a correlation coefficient of 0.64. Using the models and comparing the calculated and the measured electrons gives a correlation coefficient of 0.60. We may conclude that the correlation coefficient is maintained.

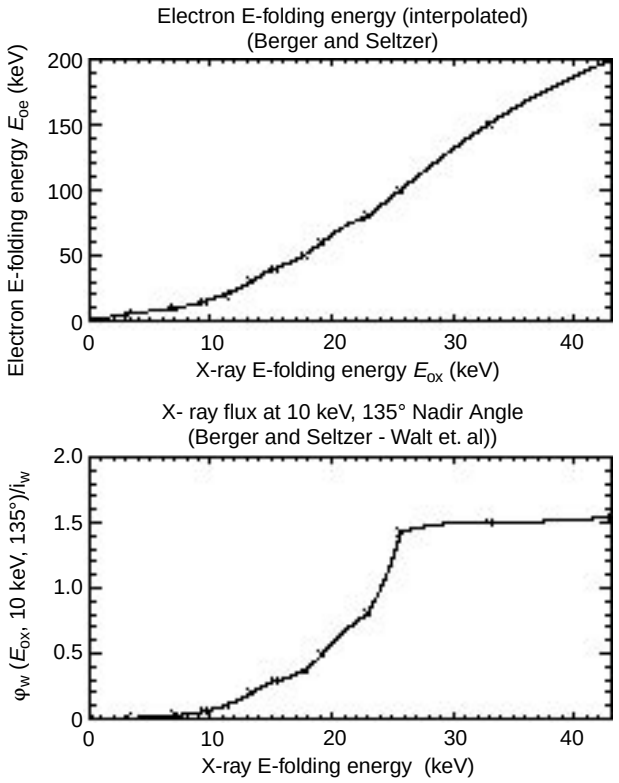

Fig. 9. Upper panel, *Crosses*: electron e-folding energies versus X-ray e-folding energies as calculated from X-ray spectra given by Berger and Seltzer, shown in Fig. 5. *Solid line*: interpolation and extrapolation for $E_{ox} = 0$–43 keV giving E_{oe} up to 200 keV, using a third-order polynomial approximation. Lower panel: the X-rays produced at 10 keV as a function of X-ray e-folding energies. *Crosses* are the values deduced from Berger and Seltzer (1974) and Walt *et al.* (1979). *Solid Line* is the third order polynomial interpolation and extrapolation

The calculated electron fluxes are 1.27 times as high as the directly measured electron fluxes. This is the averaged ratio for the time-interval from 135 to 199-s flight time.

Regarding the e-folding energies in the middle panel of Fig. 11, there is a very good match between the soft part of the calculated spectra and the derived spectra from the measurements, assuming that the integral count rates can be represented by only one exponential function. We achieve very good match for both the shape of the spectra and the magnitude of the fluxes below ~60–80 keV. There is only one significant difference in the comparison. As we have observed a hard tail in the X-ray spectra, we get a hard tail in the deduced electron spectra, as seen both in the bottom panels of Fig. 10 and the middle panel of Fig. 11. As a hard tail in X-rays may be produced by a few energetic electrons, the calculated integral electrons are not necessarily much affected by this.

The hard tail in the calculated electron spectra, resulting from the hard tail in the X-ray spectra, may indicate that the electron spectra above 25 keV cannot be represented by only one exponential function. As we do not have spectral measurements above 20 keV in this time-interval, we are not able to examine this directly. However, from the detector looking at 135° relative to rocket axis, we obtained the electron spectra before 73-s flight time for backscattered electrons above 20 keV. The rocket height was then 98 km, i.e. above the height where the energetic electrons are absorbed. In Fig. 12 the 1-s-averaged spectrum at 72–73-s flight time is shown. We do not know whether this spectrum is representative for the spectra later in the flight. Nevertheless, from this spectrum we can estimate three e-folding energies above 20 keV, as indicated in the figure. Below ~50 keV we estimate an e-folding energy of ~10 keV, above ~90 keV we estimate an e-folding energy of several hundred of keV's and in the intermediate energy range we estimate ~30 keV. As this hard tail is observed every second early in the flight, the spectrum shown in Fig. 12 strongly indicates that the electron spectra above 20 keV cannot be represented by only one exponential, but maybe by two exponentials or a different function, corresponding much better with the electron spectra we deduce from the X-ray spectra. From the electron spectra in Fig. 10, it is obvious that a small softening of the spectra above 20 keV will leave enough integral counts to incorporate a hard tail of the spectrum. This is clearly seen from both the electron spectra at 167- and 175-s flight time, and from the middle panel in Fig. 11.

Our method seems to give a good match between measured and calculated electrons. Regarding the discrepancies in the magnitude of fluxes and the shape of the spectra, they do not exceed the errors due to the uncertainties in our measurements and the geometry of the source region.

These uncertainties are mainly covered by the following.

We do not know if we were looking at the same intensity of X-rays in the chosen sector as in the rocket position. We only know that the intensity of the light recorded by the all-sky camera seems to be uniform in these two areas. This may account for some errors in our calculations.

From the calibration of the sensors in the LEES detector, we know that the count rates from the least sensitive to the most sensitive sensor may vary by about a factor of two. As the choice of unit sensor is close to the average sensitivity, the uncertainty is set to 30% of the measured fluxes.

Regarding the X-ray measurements, there are some uncertainties connected to the determination of the energy thresholds of the channels. This may lead to errors concerning both the spectral shape and the flux. The low-energy channels are most sensitive to this effect, as these energy bands are very narrow.

There are also some uncertainties in the determination of the lower energy threshold for the integral electron (HEED) detector.

7 Discussion and conclusions

Similar comparisons between precipitating energetic electrons and X-rays have been performed by others.

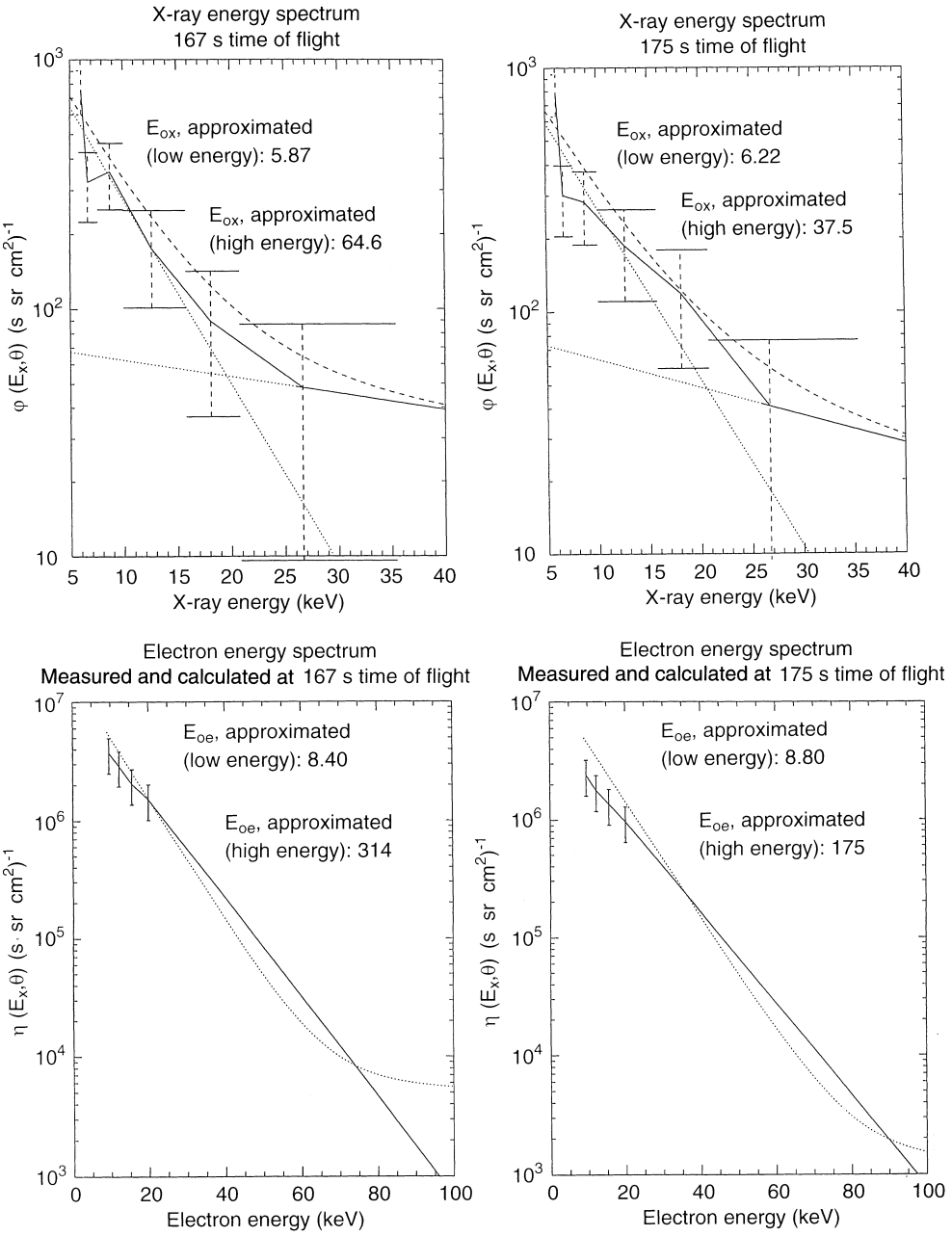

Fig. 10. The two upper panels: X-ray energy spectra for 167- and 175-s flight time, in lin-log scale. *Solid line*: measurements in azimuth sector 0° to 30°, with error bars (statistical fluctuations) indicated. The channels 10.0–12.3 keV and 12.3–15.8 keV are added. *Dotted line*: two exponential approximations. *Dashed line*: the two exponential approximations added. The two lower panels: electron energy spectra for 167- and 175-s flight time for $E_e > 10.8$ keV. *Solid line*: measurements, with error bars (30%) indicated. *Dotted line*: the calculated electron spectra calculated from the two-exponential approximations of the X-ray spectra

Data from a rocket experiment have been investigated by Vij *et al.* (1975); they calculated the X-rays produced by measured electron energy spectra. By estimating different values for the constant in the thick target theory, they got the best fit between measured and calculated X-rays above 15 keV, with uncertainties of a factor of 10. Mizera *et al.* (1978) investigated satellite measurements. They calculated X-ray spectra from electron spectra. Comparison with measured X-ray spectra gave good agreement, but with uncertainties of a factor 2–3. Datlowe *et al.* (1988) have also analysed satellite measurements of bremsstrahlung X-rays obtained over the auroral regions. X-ray spectra were measured in 20 energy channels in the 4–40-keV range. Electrons precipitating into the region of X-ray emission were not measured. The X-ray spectra were found to be consistent with both an exponential and a Maxwellian form of the incident spectrum (approximately equal goodness of fit). Energy deposition and ionization rates resulting from the inferred electron spectra were calculated.

In our study we have deduced electrons, 10.8–250 keV, from measured X-rays. Compared to the directly measured electrons we found a discrepancy of about 30%. These good results are provided by the combined use of different works that constitute a complete method to derive equivalent isotropic fluxes and spectra for the angular dependent precipitating electrons from angular-dependent X-ray measurements.

In deducing the electron spectra from the X-ray spectra, we have used a sum of two exponentials to

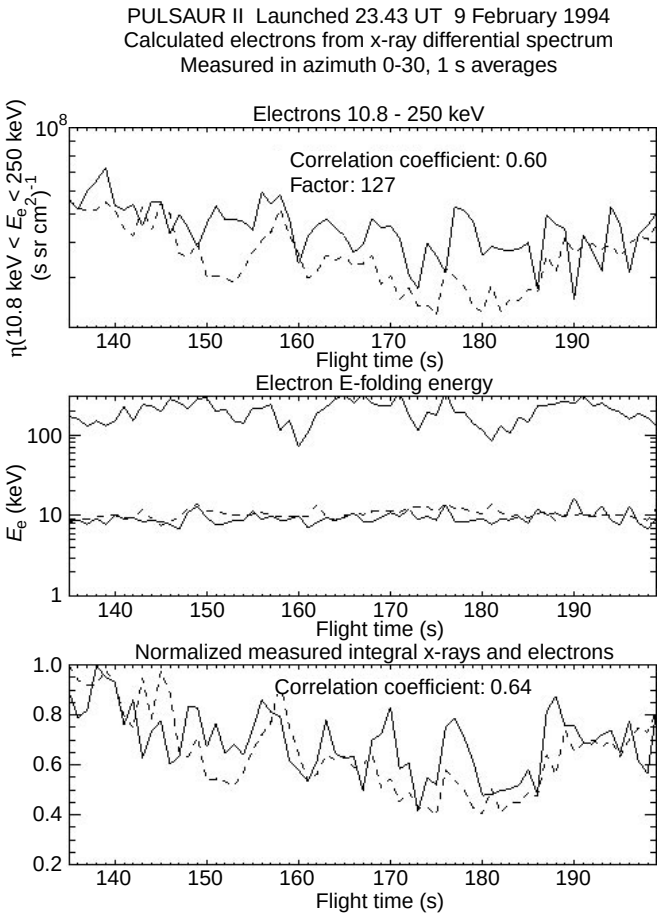

Fig. 11. Calculated electrons from differential X-ray spectra and directly measured electrons, equivalent isotropic integral fluxes. Upper panel, *Solid line*: electrons integrated from 10.8 to 250 keV, calculated from X-ray differential spectra (5.6–100 keV) measured in the azimuth sector from 0° to 30°. *Dashed line*: directly measured electrons, integrated from 10.8 to 250 keV. Middle panel, *solid lines*: electron e-folding energy, calculated from the X-ray measurements, both the soft and the hard part of the spectrum. *Dashed line*: derived electron e-folding energy, assuming that the integral count rates above 25 keV can be represented by only one exponential function. Lower panel, *solid line*: normalized (to maximum count rate) measured X-rays from 10.0 to 35.4 keV. *Dashed line*: normalized (to maximum count rate) measured electrons from 10.8 up to 250 keV

Table 3. The main results from Figs. 10 and 11

	Electrons: measured to calculated (10.8 – 250 keV)
Correlation coefficient between calculated and measured integral electrons	0.60
Correlation coefficient between directly measured integral X-rays and electrons	0.64
Flux ratio	1.27
e-folding energy below ~60–80 keV, derived from measurements and calculated from the soft part of the X-ray spectrum	Very good agreement

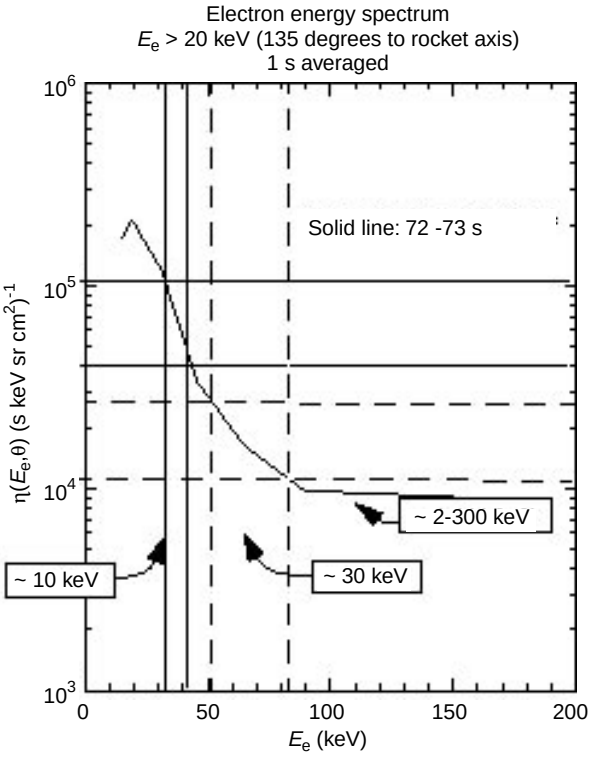

Fig. 12. Electron energy spectrum, backscattered at 72-s flight time; 1-s averaged

represent the measured X-rays. This was found to represent the X-ray spectrum quite properly and is also reported from other rocket X-ray measurements during early recovery phase (Goldberg *et al.*, 1982).

We have transposed the anisotropic fluxes to equivalent isotropic fluxes of electron precipitation, using results from the work of Mæhlum and Stadsnes (1967), as the models assume isotropic fluxes of the electrons.

We have combined two models, i.e. the model developed in Berger and Seltzer (1972) and Seltzer and Berger (1974) and that developed by Walt *et al.* (1979). By doing this we were able to take into account that the X-rays are not emitted isotropically from the production layer. The preference for horizontal escape angles is significant for all energies and most pronounced at the higher X-ray energies.

Following this procedure we have obtained a combined model deducing electrons from X-rays. The discrepancies in our calculations do not exceed the errors due to uncertainties, resulting from the instruments and the geometry of the observations.

Although our results show satisfactory agreement between observed and derived electron fluxes and spectra, there are still shortcomings in the inversion technique.

In Walt *et al.* (1979) the angular distribution of X-rays propagating out of the atmosphere is given only for five different e-folding energies of the electron spectra. In the inversion process one thus had to interpolate between these distributions and this introduces some uncertainty.

The theoretical models of Berger and Seltzer and Walt *et al*. assume an exponential shape of the electron energy spectrum. This is clearly an idealization of the real shape of the electron energy spectrum which sometimes may be fairly good but in other cases not so good at all.

Berger and Seltzer and Walt *et al*. assumed isotropic fluxes of precipitating electrons. In our case we observed an anisotropic electron precipitation. In our calculation of the equivalent isotropic electron distribution, we have assumed that the X-ray production from monoenergetic electrons is proportional to the number of electrons absorbed in the atmosphere. We do not know how good this assumption is.

Both Berger and Seltzer and Walt assume homogeneous electron precipitation over wide horizontal areas. This is most often not the case in reality, and it is clear that the geometry of the electron precipitation regions will influence the angular distribution of the X-rays leaving the atmosphere. Assuming uniform precipitation, the van Rhijn effect will influence the calculation of the angular distribution of X-rays to a large extent. In the case studied in this paper we observed both arc fragments and patches, and as the detector was looking at slant angles at the source region the van Rhijn effect will be different from the uniform precipitation case, causing some uncertainty in the calculations.

The e-folding energy obtained for the hard tail in the electron spectra are somewhat overestimated as we have represented the X-ray spectra obtained by Seltzer and Berger (1974) by a simple exponential.

We conclude that by using proper inversion procedures, the remote measurement of X-rays is a powerful technique to derive the spatial, temporal and energy distribution of the energetic electron precipitation. From this distribution it is possible to calculate the energy deposition into the atmosphere, as well as the ionization and the conductivity changes by the electron precipitation. This technique can be used at daytime as well as at night-time.

Recently the PIXIE X-ray camera on the NASA POLAR satellite (Imhof *et al*., 1995), launched in February 1996, has obtained global images of the auroral X-rays. This will provide a unique tool for making progress in the study of the dynamic interaction between magnetospheric high-energy electrons and the ionosphere, e.g. during substorms and magnetic storms.

Acknowlegements. The authors would like to thank S. Njaastad and A. Solberg, University of Bergen, for efficient management of the rocket payload, and the experiment engineers at the University of Bergen and University of Oslo for able work on the X-ray spectrometer and the photometer, respectively. We also wish to thank R. Woodliffe of MSSL, A. Preece of RAL, C. Rogers of Hughes STX, and B. Piepgrass and J. Scherrer of SwRI for their considerable efforts in various phases of fabrication, testing, and calibration of the low-energy electron spectrometer (LEES). The authors would like to thank Geir B. Håheim, University of Bergen, for assistance on the data analysis. This project was supported by the Research Council of Norway. The work at Southwest Research Institute was supported by NASA Grant NAS5-671.

References

Berger, M. J., and S. M. Seltzer, Bremsstrahlung in the atmosphere, *J. Atmos. Terr. Phys*., **34,** 85–108, 1972.

Berger, M. J., S. M. Seltzer, and K. Maeda, Energy deposition by auroral electrons in the atmosphere, *J. Atmos. Terr. Phys*., **32,** 1015–1045, 1970.

Bryant, D. A., G. M. Courtier, G. Skovli, H. R. Lindalen, K. Aarsnes, and K. Måseide, Electron density and electron flux in a glow aurora, *J. Atmos. Terr. Phys*., **32,** 1695–1970, 1970.

Datlowe, D. W., W. L. Imhof, and H. D. Voss, X-ray spectral images of energetic electrons precipitating in the auroral zone, *J. Geophys. Res*., **93,** 8662–8680, 1988.

Goldberg, R. A., J. R. Barcus, L. A. Treinish, and R. R. Vondrak, Mapping of auroral X-rays from rocket overflights, *J. Geo phys. Res*., **87,** 2509–2524, 1982.

Gorney, D. J., Satellite-based remote sensing of the aurora, in *Quantitative modelling of magnetosphere – ionosphere coupling processes*, Ed: Y. Kamide, and R. Wolf, Kyoto Sangyo University, Kyoto, Japan, 1987.

Imhof, W. L., K. A. Spear, J. W. Hamilton, B. R. Higgings, M. J. Murphy, J. G. Pronko, R. R. Vondrak, D. L. McKenzie, C. J. Rice, D. J. Gorney, D. A. Roux, R. L. Williams, J. Stein, J. Bjordal, J. Stadsnes, K. Njøten, T. J. Rosenberg, L. Lutz, and D. Detrick, The polar ionospheric X-ray imaging experiment (PIXIE), *Space Sci. Rev*., **71,** 385–408, 1995.

Kamiyama, H., Flux of bremsstrahlung photons caused by energetic electrons precipitating into the upper atmosphere, *Rep. Ionosph. Space Res. Jpn*, **20,** 374–394, 1966.

Khosa, P. N., R. R. Rausaria, and K. L. Moza, Spectrum, angular distribution and polarization of auroral hard X-rays, *Planet. Space Sci*., **32,** 31–39, 1984.

Luhmann, J. G., and J. B. Blake, Calculations of soft auroral bremsstrahlung and Ka line, emission at satellite altitude, *J. Atmos. Terr. Phys*., **39,** 913–919, 1977.

Mæhlum, B., and J. Stadsnes, Scattering and absorption of fast electrons in the upper atmosphere, *Phys Norvegia*, **2** (2), 111–122, 1967.

Måseide, K., F. Søraas, K. Aarsnes, J. Bjordal, A. Coates, W. M. Farrell, T. A. Fritz, M. P. Gough, M. Grande, J. A. Holtet, R. Pfaff, M. Smith, J. Stadsnes, K. R. Svenes, J. Trim, and R. D. Woodliffe, Pulsaur II: a sounding rocket project to study pulsating aurora and related phenomena. *Proc 12th ESA Symp European Rocket and Balloon Programmes and Related Research*, *Lillehammer*, *Norway*, 227–233, 1995.

Mizera, P. F., J. G. Luhmann, W. A. Kolasinski, and J. B. Blake, Correlated observations of auroral arcs, electrons, and X-rays from a DMSP satellite, *J. Geophys. Res*., **83** (A12), 5573–5578, 1978.

Omholt, A., *The Optical Aurora*, Springer, Berlin, Heidelberg, New York, 1971.

Robinson, R. M. and R. R. Vondrak, Validation of techniques for space based remote sensing of auroral precipitation and its ionospheric effect, *Space Sci. Rev*., **69,** 331–407, 1994.

Robinson, R. R., G. T. Davidson, R. R. Vondrak, W. E. Francis, and M. Walt, A technique for interpretation of auroral bremsstrahlung X-ray spectra, *Planet. Space Sci*., **37,** 1053–1062, 1989.

Rees, M. H., Ionization in the earth's atmosphere by aurorally associated bremsstrahlung X-rays, *Planet. Space Sci*., **12,** 1093–1108, 1964.

Seltzer, S. M., and M. J. Berger, Bremsstrahlung in the atmosphere at satellite altitudes, *J. Atmos. Terr. Phys*., **36,** 1283–1287, 1974.

Sharber, J. R., J. D. Winningham, J. R. Scherrer, M. J. Sablik, C. A. Bargainer, P. A. Jensen, B. J. Mask, N. Eaker, and J. C. Biard, Design, construction, and laboratory calibration of the angle resolving energy analyser (AREA): a "top-hat" instrument for auroral research. *IEEE Trans. Geosci. Rem. Sensing*, **26** 174–486, 1988.

Søraas, F., K. Aarsnes, J. Bjordal, J. Stadsnes, K. Måseide, M. F. Smith, and U. P. Løvhaug, Pulsaur II: rocket and groundbased

measurements in a pulsating aurora, *Proc. 12th ESA Symp. European Rocket and Balloon Programmes and Related Research*, *Lillehammer*, *Norway*, 233–237, 1995.

Stadsnes, J., K. Aarsnes, J. Bjordal, F. Søraas, and K. Måseide, Pulsaur II: observations of aurora and brems-strahlung X-rays in a pulsating aurora, *Proc. 12th ESA Symp. European Rocket and Balloon Programmes and Related Research*, *Lillehammer*, *Norway*, 239–243, 1995.

Vij, K. K., D. Vekatesan, W. R. Sheldon, J. W. Kern, J. R. Benbrook, and B. A. Whalen, Simultaneous investigation of parent electrons and bremsstrahlung X-rays by rocket-borne detectors, *J. Geophys. Res.*, **80,** 2869–2875, 1975.

Walt, M., L. L. Newkirk, and W. E. Francis, Brems-strahlung produced by precipitating electrons, *J. Geophys. Res.*, **84,** 967–973, 1979.